It takes two to tango – double-layer selective contacts for improved device performance and reduced hysteresis in perovskite solar cells

Lukas Kegelmann[1]*, Christian Wolff[3], Celline Awino Omondi[1], Felix Lang[1], Eva Unger[1,4], Lars Korte[1], Thomas Dittrich[1], Dieter Neher[3], Bernd Rech[1],Steve Albrecht[2]*

[1] Helmholtz-Zentrum Berlin, Institute Silicon Photovoltaics, Berlin, 12489, Germany.

[2] Helmholtz-Zentrum Berlin, Young Investigator Group Perovskite Tandem Solar Cells, Berlin, 12489, Germany.

[3] University of Potsdam, Soft Matter Physics, Potsdam, 14476, Germany.

[4] Division of Chemical Physics, Department of Chemistry, Lund University, Lund, 124, Sweden.

* Corresponding authors.

Abstract

Perovskite solar cells gradually approach market requirements as efficiency and stability improved tremendously in recent years. Planar low-temperature processed devices without a mesoscopic scaffold are advantageous for a possible large-scale production but often suffer from photocurrent hysteresis, especially in the regular *n-i-p* structure. Here, we systematically utilize different low-temperature deposited electron transport materials (ETM) with a variety of chemical and electrical properties in a planar regular architecture. We perform scanning electron microscopy and surface photovoltage spectroscopy to show very comparable absorber growth on all examined ETMs. Transient photoluminescence studies together with current-voltage scans over a broad range of scan speeds revealed better charge extraction, faster and less pronounced hysteretic effects and higher efficiencies for devices with fullerene compared to metal oxide ETMs. We further show that a double-layer ETM design can substantially diminish hysteresis effects and strongly enhance the power conversion efficiency up to a champion stabilized value of 18.0 %. The results indicate reduced recombination losses for a TiO_2/PCBM contact design and we suppose multiple beneficial effects as the originating charge transport mechanisms: reduction of shunt paths through the fullerene to the ITO layer, improved hole blocking by the wide band-gap metal oxide and decreased charge transport losses due to an energetically more favorable contact as implied by photoelectron spectroscopy.

Introduction

In recent years, inorganic-organic perovskite solar cells obtained remarkable power conversion efficiencies above 22 % and hence are already on level with the record values of CdTe and $Cu(In,Ga)Se_2$ (CIGS),[1] the two major technologies in thin film photovoltaics.[2] Although long-term stability of the perovskite devices is still an obstacle towards market introduction,[3] significant progress was recently achieved for example by improving the intrinsic stability of the perovskite absorber via a robust quadruple-cation composition[4] or by additional protection layers to avoid moisture ingress or UV light induced degradation.[5,6] Prototype photovoltaic modules or the acquisition of pilot development lines to scale-up the technology already signified the first steps towards commercialization of perovskite solar cells.[7,8] With the perspective of a potential large-scale production, low-temperature processed planar perovskite solar cells provide cheaper and simpler manufacturing than high temperature sintered mesoscopic architectures. They furthermore offer a wide range of application also on thermally limited substrates like flexible foils[9,10] or bottom cells in monolithic tandem devices.[11–13] However, especially the planar regular *n-i-p* structure is supposed to suffer more severely from hysteretic effects than mesoscopic or inverted *p-i-n* architectures.[14–17]

Charge selective contacts, especially fullerene derivatives, were shown to provide the potential of reducing photocurrent hysteresis.[17–19] Thus we investigate the influence of different low-temperature deposited organic and inorganic electron transport materials (ETM) on the performance

and hysteresis of planar regular perovskite solar cells. In order to isolate the impact of the ETM properties on device characteristics, we keep all processing steps beside the ETM-layer unmodified. We additionally use a perovskite deposition method which is hardly affected by the underlying substrate as we show by scanning electron microscopy and surface photovoltage spectroscopy. The substrate unaffected deposition method enables to establish a unique relation between device performance and ETM-contact properties. Transient photoluminescence and current-voltage measurements at different scan speeds revealed faster and less pronounced hysteretic responses as well as higher stabilized efficiencies for devices with fullerene compared to metal oxide ETMs. However while also numerous other reports focus on optimizing the charge selective material interfacing the perovskite,[20–22] we further show that an additional interlayer not in direct contact to the perovskite absorber can have major beneficial effects. By depositing metal oxides between the ITO electrode and a fullerene electron selective contact, we successfully reduce hysteresis effects and strongly improve the power output by ca. 30 % in average and up to a stabilized champion device efficiency of 18.0 %. Supported by photoelectron spectroscopy, we relate the improved efficiencies to reduced recombination losses throughout the electron contact and suggest minimized shunt paths, improved hole blocking properties and enhanced charge transport from the fullerene to the electrode to be the originating enhancements.

Results and discussion

In this study, we analyze the effect of different electron transport materials (ETMs) on perovskite solar cell characteristics in a planar *n-i-p* superstrate structure as shown in Figure 1 (a). Various ETMs that are processed at temperatures below 180 °C, are coated onto ITO covered glass substrates followed by the perovskite layer, Spiro-OMeTAD as a hole selective contact and a gold electrode. Further, we extend the device structure to a double-layer electron contact design by using a metal oxide and a fullerene derivative (PCBM) as depicted in Figure 1 (b).

The examined ETMs range from inorganic metal oxides such as titanium dioxide (TiO_2) and tin oxide (SnO_2) fabricated according to reported protocols,[23,24] to the organic fullerene C_{60} and its derivatives PCBM and ICMA. TiO_2 is the predominantly used ETM in mesoscopic perovskite solar cells,[14,17] but the reported poor charge extraction properties[25] possibly make this material less suitable for planar thin film devices with limited contact area to the absorber, especially when being processed at low temperatures with limited crystallinity. Promising alternatives are SnO_2 due to its wide band gap and high electron mobilities,[24] but also fullerenes as they provide good charge extraction properties[26,27] and additionally are supposed to passivate defects at the perovskite surface.[28] Both can lead to reduced recombination losses at the interface and hence improve device performance and suppress photocurrent hysteresis.[29]
However, to the best of our knowledge ICMA has not yet been applied in perovskite solar cells. It has though been used in organic photovoltaics[30] as a fullerene derivative with different energy levels than C_{60} or PCBM due to its comparable chemical structure but with a different side group attached to the spherical C_{60}.[31]
The poor electron extraction from perovskite absorbers to TiO_2 can also be remedied via interface modifications for example by C_{60}-monolayers[25] or TiO_2/PCBM double-layer electron contacts.[27] However, in these cases the electron selective materials interfacing the perovskite are the same as for C_{60} or PCBM single-layer ETMs. To elucidate the role of the underlying TiO_2, we vary TiO_2 and SnO_2 in a metal oxide/PCBM double-layer structure and compare it to devices incorporating PCBM single-layer ETMs. Note that cathode buffer layers between PCBM and the electrode are often used in inverted solar cells to potentially increase the shunt and decrease the series resistance of the devices[14,32] but are rarely utilized in the regular architecture.

A scanning electron microscope (SEM) image presented in Figure 1 (c) illustrates the cross section of a representative perovskite solar cell used in this study with a single-layer electron contact of PCBM. The device stack of ITO/PCBM/CH$_3$NH$_3$PbI$_3$/Spiro-OMeTAD/gold is clearly distinguishable with layer thicknesses around 150 nm, 30-40 nm, 350 nm, 200 nm and 80 nm, respectively. It can also be seen that most grains of the perovskite absorbers are not vertically elongated throughout the complete film thickness and horizontal grain boundaries are visible.
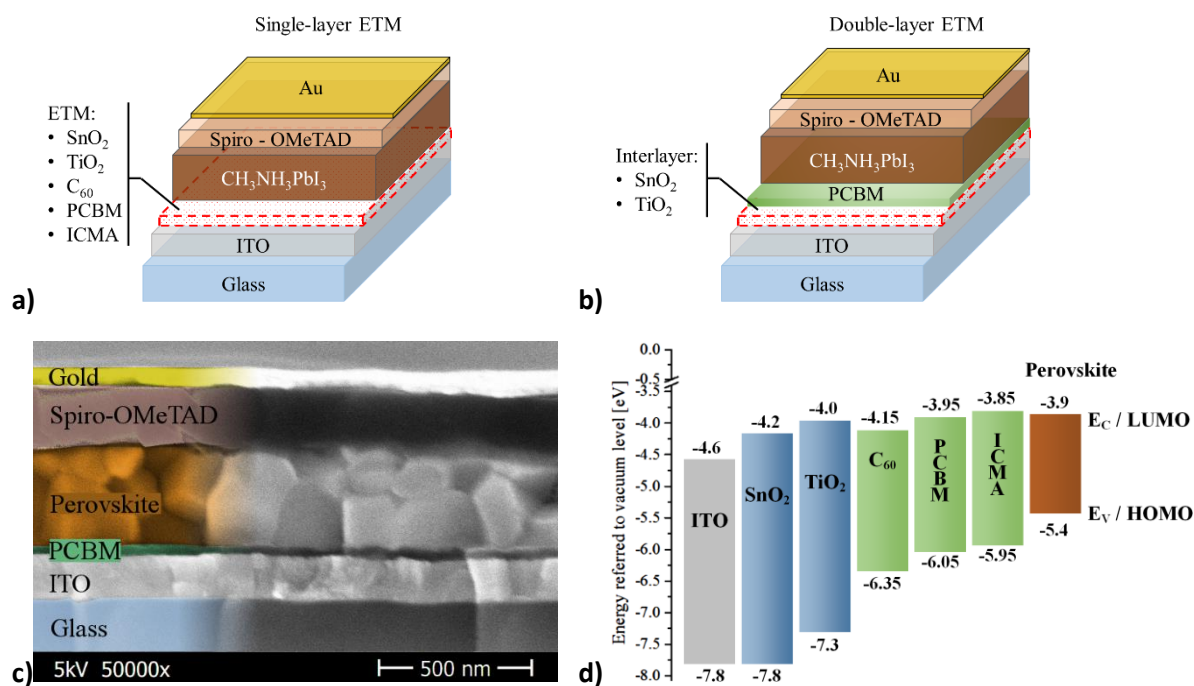

Figure 1. Schematic illustration of the device architecture with (a) single-layer and (b) double-layer electron contact structure. (c) SEM cross section image of a perovskite solar cell with PCBM as single-layer electron transport material (ETM). (d) Energy level scheme of the studied materials. Valence band (E$_V$) and HOMO energies were determined by UPS, conduction band (E$_C$) and LUMO levels are estimated by subtracting reported band gap values from the measured E$_V$ or HOMO data.[31,33–35] Perovskite energy levels were obtained from literature.[36]

In general, an electron transport material has to extract electrons and block holes from a photoactive absorber to be highly selective. We analyzed the energy levels of the valence bands (E$_V$) and highest occupied molecular orbitals (HOMO) by ultraviolet photoelectron spectroscopy (UPS) and the respective energies of the conduction bands (E$_C$) and lowest unoccupied molecular orbitals (LUMO) were approximated by subtracting reported band gap energies of the materials from the E$_V$/HOMO values.[31,33–35] The results are depicted in Figure 1 (d) along with energy levels of CH$_3$NH$_3$PbI$_3$ obtained from literature.[36]

As displayed in Figure 1 (d), the ETMs used in this study provide a diverse range of energy levels. The wide band gap metal oxides have around 2 eV larger ionization energies than the perovskite absorber which should lead to distinct extraction barriers for holes at the interface. Fullerenes on the other hand have more than 1 eV lower ionization energies than the metal oxides and therefore also the hole blocking probability should be notably decreased. The approximated electron affinities of the ETMs as displayed in Figure 1 (d) appear to be graduated over around 300 meV between -3.85 to -4.2 eV. A 200 meV difference in E$_C$ values is distinguishable between the metal oxides SnO$_2$ and TiO$_2$, which can have significant influence on the device performance.[33] Besides, for each metal oxide a respective fullerene with comparable electron affinities was used in this study, namely C$_{60}$ (-4.15 eV) for SnO$_2$ (-4.2 eV) as well as PCBM (-3.95 eV) for TiO$_2$ (-4.0 eV). All aforementioned

materials are supposed to have higher electron affinities than the perovskite absorber and should therefore avert energetic barriers for electrons being extracted from the perovskite into the ETM. ICMA however with the lowest electron affinity of approximately -3.85 eV could induce a small electron extraction barrier when interfacing the perovskite.

We additionally analyzed the energy levels for the double-layer ETM architecture. UPS measurements revealed no substantial differences with only 50 meV higher ionization energies for PCBM layers deposited on TiO_2/SnO_2 (double-layer ETM) compared to PCBM on ITO (single-layer ETM) (Table S1, supporting information). Therefore we suppose that any changes in device performance between the PCBM single and the $TiO_2/PCBM$ double-layer are not significantly affected by energy level differences.

Thus the numerous ETMs used in this study cover a wide range of material and surface properties. When comparing solar cells made on different ETMs, we have to consider that topography and chemical properties of the underlying surface can significantly influence the perovskite absorber grown on top.[37] The "One-Step" deposition method used here with anti-solvent drip during spin coating[38] first leads to a transparent intermediate phase layer. Perovskite nuclei are formed in the bulk or the surface of this preliminary film or at the ETM surface and grains afterwards grow from these nuclei during thermal annealing.[16] Differences in the surface roughness or the chemical properties of the underlying layer usually change the interfacial energies[39] and thereby the nucleation dynamics on top of it as well as the wetting properties and contact angles of the precursor solution.[40]

The polar perovskite precursor solution used here showed good wetting properties with small contact angles on top of the polar metal oxide surfaces, but significantly larger values on the non-polar fullerenes PCBM and ICMA (see Figure S2). The contact angle on the evaporated C_{60} was considerably smaller than on the aforementioned spin-coated fullerene derivatives which might be related to the different deposition method or the distinctly higher root-mean-square surface roughness of around 16 nm for C_{60} versus 4 nm for PCBM (Table S2).
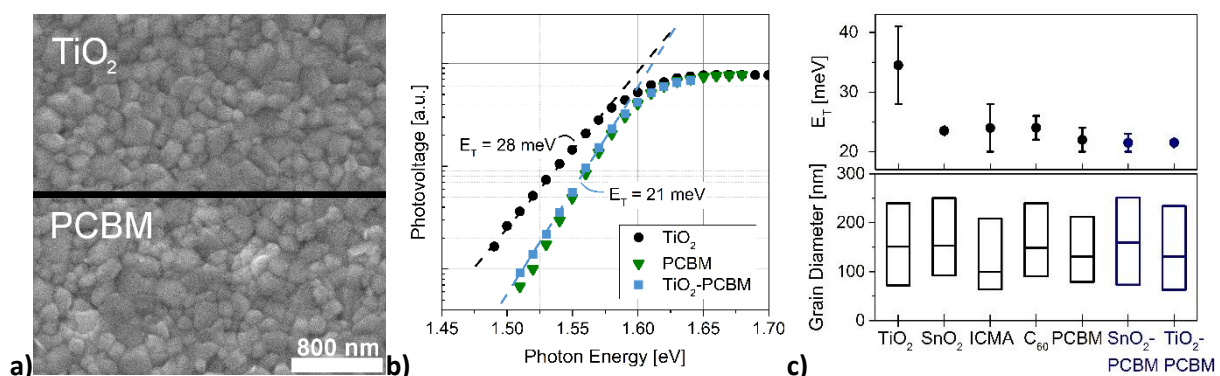

Figure 2. (a) Top view scanning electron microscopy (SEM) images of perovskite absorbers on substrates coated with TiO₂ (top) and PCBM (bottom). (b) Surface photovoltage (SPV) spectra and fits to the tail state energies Eₜ of perovskite absorbers on substrates with TiO₂ and PCBM single- as well as TiO₂-PCBM double-layer electron transport material (ETM). (c) Top panel: tail states energies Eₜ from SPV measurements of perovskite absorbers grown on different ETM coated substrates. The error bar is defined by the standard deviation. Bottom panel: box plot diagram of the grain size distribution for perovskite surfaces on different underlying ETM determined by SEM.

Despite these large differences in contact angles and thereby interfacial energies, SEM top view images of annealed perovskite absorber surfaces on the various ETMs did not show significant

differences in grain sizes as exemplarily shown in Figure 2 (a) for TiO_2 and PCBM coated substrates. The grain size distribution from these top view images is depicted as a box plot in the lower panel of Figure 2 (c), revealing an average perovskite grain diameter for all samples of around 150 nm with slightly lower values for ICMA based devices. Besides that, SEM cross section images revealed a prominent appearance of horizontal grain boundaries as described before. Note that very high solar cell performance have been demonstrated for evaporated perovskite layers with even much smaller grains by elaborate contact optimization.[41] Both, the unaffected grain size when being processed on different ETMs and the indication of horizontal grain boundaries, indicate that an apparent amount of perovskite nuclei are formed within the bulk or at the surface of the intermediate phase film. The nucleation dynamics on the ETM surface thus seem to only partially contribute to the overall film formation. This finding is supported by previous reports, showing that anti-solvent treatment induces crystallization at the surface of a precursor liquid.[42] Therefore the perovskite film formation protocol applied here is highly useful for studying the differences in device performance when using different ETMs as the coarse film morphology seems to be independent of the specific ETM used.

In order to characterize the absorber quality in more detail, we performed surface photovoltage (SPV) measurements to determine the tail state energies E_T of perovskite layers on different ETMs. The spectral gradient of the surface photovoltage when a semiconductor is excited with light at wavelengths around the band gap energy provides insights into charge separation processes via energetic states within the band gap.[43] Small E_T values indicate higher electrically ordered absorbers with low sub-bandgap trap densities near the band edge and therefore reduced recombination losses which is in general beneficial for the device performance.[44]

We prepared several batches of perovskite layers on glass/ITO/ETM substrates and determined the respective E_T values. On all substrates apart from TiO_2, the average tail state energies were comparable with medium values of 22 to 24 meV (Figure 2 (c), top panel) and lowest energies for each ETM around 20 meV, as exemplarily depicted for PCBM and TiO_2-PCBM samples in Figure 2 (b). This further promotes the assumption of a minor influence of the underlying substrate on the perovskite absorber grown on top. SPV characteristics of specimens with TiO_2 as ETM in contrast revealed much higher E_T values of 35 meV in average (Figure 2 (c), top panel) and 28 meV for the sample with the minimum E_T (Figure 2 (b), black dots). However the large standard deviation as well as the high mean value of the tail state energies for perovskites on glass/ITO/TiO_2 might be related to a substantial density of shallow traps in the TiO_2 which allows excitation of charge carriers from the perovskite valence band into TiO_2 defect states at the interface.[45]

To sum up, we have shown highly diverse material properties and energy levels of the used ETMs but rather similar perovskite absorbers on top, as the coarse morphology and the perovskite tail state energies (despite for bare TiO_2 samples) were found to be comparable. Because also the remaining top contact layers of the solar cells are identical, we can directly refer differences in device parameters to variations of the ETM. Hence, we performed transient photoluminescence (TRPL) measurements to study the charge carrier dynamics for perovskite solar cells with different ETMs in the single- and double-layer design. The TRPL signal stems from radiative recombination of excited charge carriers in the absorber and can therefore be quenched by either efficient charge extraction or increased non-radiative recombination.
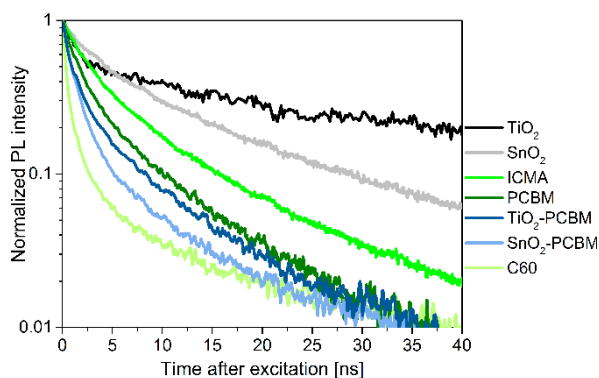
Figure 3. Normalized transient photoluminescence (TRPL) decays for perovskite solar cells with different electron transport materials (ETMs) measured without applying external bias.

As shown in Figure 3, fullerene ETM layers quench the photoluminescence signal stronger than metal oxide interfaces, which is in agreement to previous reports that C_{60} and its derivatives provide good electronic coupling to and efficient electron transfer from perovskite absorbers.[26,27] As mentioned before, poor charge extraction of TiO_2 on the other hand was suggested elsewhere[25] and seems to be confirmed by the slow decline of the corresponding TRPL signal in Figure 3 (black line). Interestingly, within the fullerenes as well as within the metal oxides, the TRPL decay seems to be faster for higher electron affinities of the ETM according to Figure 1 (d). SnO_2 for example shows a faster TRPL decay and has an around 200 meV higher electron affinity than TiO_2. Also within the group of fullerenes, C_{60} with the highest and ICMA with the lowest electron affinity exhibited the fastest and slowest TRPL quenching respectively. Lower lying LUMOs or conduction bands of the ETMs might lead to stronger electrostatic driving forces for charge extraction at the interface to the perovskite absorber.[46] However a detailed investigation of the interface energetics with possible band bending or surface dipole effects is subject of future projects and beyond the scope of this work.

When progressing from the PCBM only to the double-layer ETM architecture, a comparable decay was observed for a TiO_2 interlayer and a slightly faster one for SnO_2. The stronger quenching for the latter device design is interesting, as UPS measurements did not reveal significant deviations in the energetics of PCBM only, SnO_2/PCBM or TiO_2/PCBM surfaces (Table S1) and also the electronic coupling to the perovskite should be in all three cases dominated by PCBM molecules. However, we cannot exclude different structural ordering of the PCBM molecules when being processed either on ITO, ITO/SnO_2 or ITO/TiO_2 which could influence the device performance.[47] Still, no significant differences in charge extraction properties are indicated by TRPL for the double-layer compared to the PCBM single-layer ETM design.

To further characterize the influence of the distinct ETMs on device characteristics, we eventually investigate the electrical properties of perovskite solar cells. More than 90 different devices were prepared and examined in multiple batches over several weeks to achieve reliable trends and avoid stochastic variations by hidden or hardly controllable process parameters, such as the chemical composition or the temperature of the atmosphere during preparation. Current density-voltage (J-V) scans and maximum power point (MPP) tracking measurements of the devices under illumination were performed and the results are shown in Figure 4 (a)-(c).

Light J-V-curves in forward (from short- to open-circuit conditions) and reverse (from open- to short-circuit conditions) scan direction are exemplarily shown in Figure 4 (a) for devices based on TiO_2 and PCBM single- as well as TiO_2/PCBM double-layer ETMs. Besides also the maximum power point (MPP) after 60 s of MPP tracking measurements for each sample is depicted. The devices displayed are representative for the according ETM design as they possessed J-V parameters close to the respective average values. A significant reduction of photocurrent hysteresis and improved stabilized efficiency is observed when replacing TiO_2 with PCBM and even more for the double-layer contact design of the two materials. Also the champion device of this study depicted in Figure 4 (b) was achieved on the TiO_2/PCBM double-layer ETM. The inset shows the MPP tracking measurement with the power output stabilizing at 18.0 % within seconds and retaining this efficiency for minutes. The average device characteristics under illumination for all ETMs used in this study are displayed in Figure 4 (c) and are presented together with the champion device parameters in Table 1.

Figure 4 (c) shows the power conversion efficiency (PCE) averaged separately for reverse and forward scans over all samples at 1666 mV/s sweep rate with circles marking the power output after 60 s of MPP tracking. The data points are averaged over at least 10 devices per ETM. Regarding the single-layer structure, it can clearly be seen that the metal oxides show high efficiencies between 14 and 16 % in the reverse scans only, with very moderate values below 9 % when measured in forward direction. During MPP tracking, the PCE adversely approaches the one of the reverse scan and drops to an average of 7.0 and 10.5 % for TiO_2 and SnO_2 respectively. The fullerenes on the other hand show lower PCEs in the reverse scan than the metal oxides but the power output stabilizes closer to the MPP of the backward than of the forward sweep. ICMA provided an average PCE after 60 s MPP-tracking of 11.9 %, C_{60} and PCBM gave the best efficiencies for the single-layer structures at 12.9 and 12.7 % respectively. Note that no correlation between the energy levels, the TRPL decays and the device performance was found in this study.

When comparing solar cells with double- and PCBM single-layer ETM design, it can be seen that a SnO_2 interlayer only slightly improved the average efficiencies after 60 s of MPP-tracking to 13.5 %. TiO_2 based double-layers on the contrary significantly boosted the PCE to 16.1 % averaged over 16 devices and up to 18.0 % for the champion device of this study. The TiO_2 interlayer improved all device parameters (J_{SC}, FF, V_{OC}), whereas the SnO_2/PCBM based devices only showed higher J_{SC} but comparable FF in the reverse scan and even lower V_{OC} values compared to the PCBM single-layer solar cells (Table 1).

Improved device performances for double-layer ETM based solar cells imply decreased recombination losses. One reasonable enhancement of the inserted metal oxide layer is a reduction of shunt paths as it hampers direct contact between the perovskite absorber and the ITO electrode through pinholes in the PCBM layer. Additionally, as the wide band gap metal oxides have significantly higher ionization potentials than the fullerenes, they might support the hole blocking properties and increase the selectivity of the electron contact in the double-layer architecture. Although the aforementioned arguments are applicable for both metal oxides, significant improvements in efficiency were only obtained for TiO_2 interlayers. As the electron affinities of TiO_2 and PCBM are comparable (Figure 1 (d)), the resultant double-layer structure potentially forms an energetically more favorable contact than the SnO_2/PCBM double- or ITO/PCBM single-layer ETM design. This would result in reduced recombination losses and improved charge extraction[48] which is in agreement to the enhanced V_{OC}, FF and J_{SC} values of the TiO_2/PCBM devices compared to not only the PCBM single- but also the SnO_2 double-layer structure (Table 1).
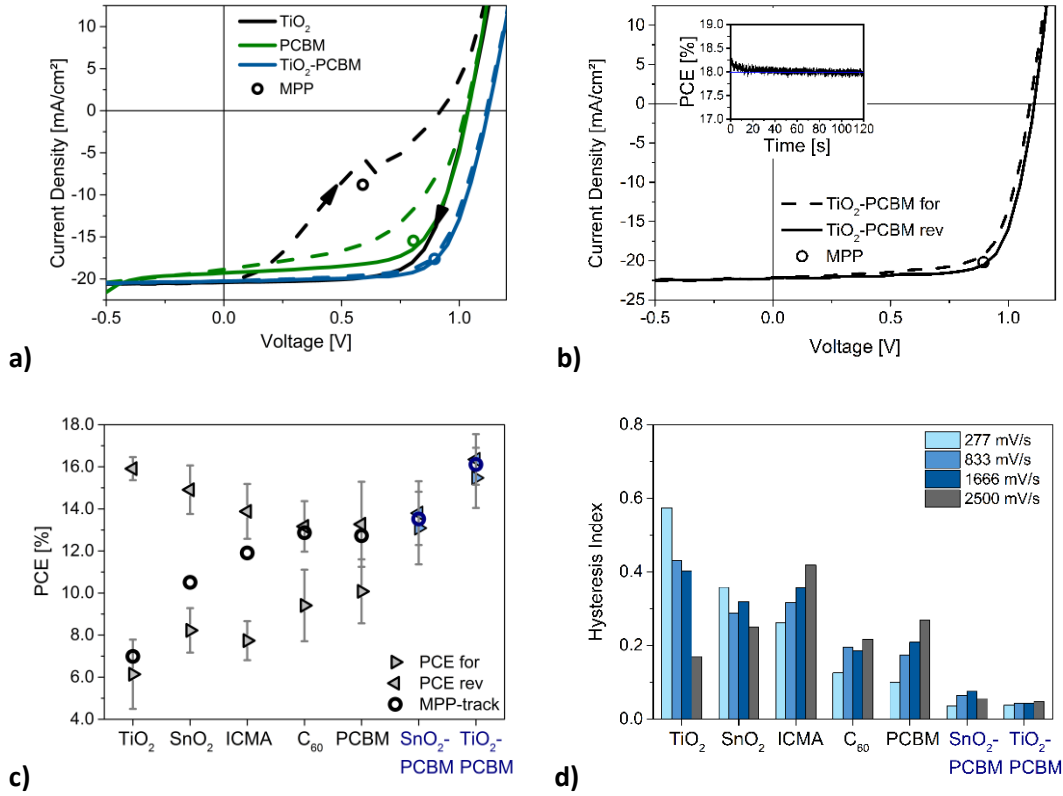
Figure 4. (a) Current Voltage characteristics under illumination for perovskite solar cells with TiO₂ and PCBM single- as well as the corresponding TiO₂-PCBM double-layer ETM structure at 1666 mV/s scan speed. Circles mark the maximum power point (MPP) after 60 s of MPP tracking measurements. The depicted devices possessed J-V parameters (J$_{SC}$, FF, V$_{OC}$, H) close to the respective average values. (b) Champion device current voltage characteristics measured under illumination at 1666 mV/s scan speed with 0.1 cm²aperture mask using a TiO₂-PCBM double-layer ETM. The inset shows the power conversion efficiency (PCE) during MPP tracking with the circle marking the corresponding stabilized MPP in the J-V-plot. (c) Efficiency of the forward and reverse scans at 1666 mV/s scan rate as well as after 60 s of MPP tracking measurements for perovskite solar cells under illumination with different ETMs averaged over all devices. (d) Hysteresis index calculated for different scan rates and averaged over all devices of the respective ETM (typically ≥10).

For a more detailed analysis of transient effects, we calculate the hysteresis index H of each current density - voltage (J-V) scan given by equation (1) following a reported approach[49], where J_{for} and J_{rev} is the current density during forward and reverse sweep respectively.

$$H = \frac{\int_0^{Voc} J_{rev}(V)dV - \int_0^{Voc} J_{for}(V)dV}{\int_0^{Voc} J_{rev}(V)dV} \tag{1}$$

It has been shown that hysteresis can be governed by multiple transient processes occurring on different timescales and thus strongly depends on the speed of the current-voltage scan.[50,51] We therefore extend the application of the hysteresis index to a broader range of sweep rates from 277 to 2500 mV/s during electrical characterization to provide better insights into the hysteretic dynamics of the different architectures used here.

The H indices for each single and double-layer ETM and scan speed shown in Figure 4 (d) present the average values over at least 10 devices of the respective contact design. It can clearly be seen that a simple comparison of this index at one sweep rate is not very informative. At the fastest scan speed

for example, devices with a TiO_2 single-layer show less hysteretic response than those with PCBM while it is vice versa for the slowest sweep rate. The depiction of H over a broader range of measurement speeds on the other hand reveals significant deviations in the dynamics of the hysteresis between samples with metal oxide and fullerene single-layer ETMs. A strong hysteresis effect at slow scan speeds can be observed for the metal oxides along with a decline of the H index for faster measuring rates while the fullerenes in contrast show the smallest hysteresis at 277 mV/s sweeps and an increase of the hysteretic response with higher sweep rates.

This indicates that pronounced hysteresis occurs on much longer timescales for devices with metal oxide ETMs and the underlying processes are too slow to respond to the faster scan speeds. Slow processes are also observed for these devices during MPP tracking measurements, where the power output does not reach a stable value even after several minutes (see inset in Figure S3 (a)). It is unclear though if the same slow process is the origin of both transient behaviors observed or if there are multiple overlaying phenomena. For solar cells incorporating fullerenes on the other hand, the increase of H with the scan speed reveals much faster hysteretic processes that can still respond at the highest sweep rate performed here. The devices also reached a stable PCE within seconds and showed no significant reduction in efficiency over several minutes of MPP tracking (see inset in Figure S3 (b)).

Fast transients of the J-V-response occurring within seconds have been attributed before to electrode polarization based capacitive effects due to accumulation of ions and photogenerated free carriers at the electrodes. [52,53] Slower transients in the timescale of minutes on the other hand have been ascribed to ion migration induced modifications of the interface energetics.[52,53] The slow charge extraction of the metal oxide ETMs indicated by TRPL is supposed to result in a large capacitance due to increased electron accumulation at the ETM/perovskite interface.[52] This is in agreement to the response limit of the hysteretic processes being at slower scan speeds compared to devices incorporating fullerene ETMs with better charge extraction properties and therefore potentially lower capacitance values.[53] Moreover, the defect passivation properties of the fullerenes might suppress the effect of interfacial ionic accumulation which further reduces capacitive processes as well as interface modifications[52] as indicated by negligible slow transients during MPP tracking. The still apparent hysteresis at fast scan speeds however is contradictory to the case of *p-i-n* devices incorporating fullerene electron contacts, which often show negligible current-voltage hysteresis.[14–16] One possible explanation for this discrepancy could be the reduced contact area in a planar *n-i-p* compared to the *p-i-n* structure where PCBM is suspected to penetrate into the perovskite absorber through pinholes and grain boundaries during processing,[54] which can even lead to graded heterojunction interfaces between perovskite and PCBM.[55]

The double-layer ETM structures in comparison exhibit strongly differing transient properties than the metal-oxide or fullerene single-layer devices. The magnitude of the hysteresis index in the studied scan speed range is dramatically reduced when the double-layer is utilized. Additionally, the dependence of H on the sweep rate is significantly smaller and hardly observable for solar cells incorporating TiO_2/PCBM electron contacts. Also during MPP-tracking, the power output stabilizes quickly and retains efficiency throughout the measurements (see inset in Figure S3 (c)). The suppressed photocurrent hysteresis can at least partially be attributed to the decreased recombination losses discussed before.[29] However, also a further reduced electrode polarization effect seems reasonable as previous reports have shown considerably smaller capacitive currents for devices with TiO_2/PCBM compared to PCBM only electron contacts.[17,53] A possible explanation for the reduced capacitance is given by Zhang et al., where the metal oxide interlayer is supposed to decrease the interface charge accumulation by acting as an additional dielectric material

incorporated between the plates of a capacitor, in this case the ITO electrode and the accumulation layer of mobile ions or free carriers.[56]

Table 1: Parameters extracted from current voltage characteristics under illumination including standard deviations corresponding to Figure 4 (b) and (c) averaged over at least 10 devices per ETM measured at 1666 mV/s scan speed in forward and reverse scan direction together with the stabilized power output from maximum power point (MPP) tracking after 60 seconds.

Electron transport material	Scan direction	J_{SC} [mA/cm²]	FF [%]	V_{OC} [V]	PCE [%]	PCE after 60 s of MPP tracking [%]
TiO$_2$	Forward	22.1 ± 0.6	29.5 ± 7.2	0.94 ± 0.04	6.1 ± 1.6	7.0 ± 1.8
	Reverse	22.3 ± 0.6	67.8 ± 1.4	1.05 ± 0.01	15.9 ± 0.5	
SnO$_2$	Forward	21.9 ± 0.8	37.3 ± 4.3	1.01 ± 0.07	8.2 ± 1.1	10.5 ± 0.9
	Reverse	22.2 ± 0.9	62.4 ± 4.7	1.08 ± 0.03	14.9 ± 1.2	
ICMA	Forward	18.7 ± 1.5	40.4 ± 5.8	1.03 ± 0.03	7.7 ± 0.9	11.9 ± 0.9
	Reverse	20.0 ± 1.2	64.7 ± 2.5	1.07 ± 0.02	13.9 ± 1.3	
C$_{60}$	Forward	19.4 ± 1.2	47.3 ± 8.3	1.03 ± 0.04	9.4 ± 1.7	12.9 ± 1.2
	Reverse	19.9 ± 1.3	62.9 ± 4.1	1.05 ± 0.02	13.2 ± 1.2	
PCBM	Forward	18.4 ± 1.9	51.5 ± 7.1	1.07 ± 0.03	10.1 ± 1.5	12.7 ± 1.8
	Reverse	19.0 ± 2.1	64.6 ± 3.6	1.08 ± 0.04	13.3 ± 2.0	
SnO$_2$-PCBM	Forward	20.1 ± 1.1	62.1 ± 5.3	1.04 ± 0.05	13.1 ± 1.7	13.5 ± 1.6
	Reverse	20.3 ± 1.1	64.7 ± 3.3	1.04 ± 0.04	13.8 ± 1.5	
TiO$_2$-PCBM	Forward	21.4 ± 1.2	65.5 ± 4.3	1.10 ± 0.03	15.4 ± 1.5	16.1 ± 1.1
	Reverse	21.5 ± 1.0	68.5 ± 2.4	1.11 ± 0.03	16.4 ± 1.3	
TiO$_2$-PCBM champion[1]	Forward	22.17	71.4	1.09	17.3	18.0
	Reverse	22.23	74.6	1.11	18.4	

[1] measured with 0.1 cm² aperture mask.

Conclusions

In summary, we have analyzed the perovskite properties and the device performance by utilizing a variety of different electron transporting materials (ETMs) in a planar *n-i-p* perovskite solar cell structure including single- and double-layer ETM designs. We showed by SEM images and surface photovoltage measurements that the used perovskite fabrication process results in absorber layers with rather similar grain growth and comparable tail state energies independent of the utilized ETM. With that, we could directly correlate the device performance and photocurrent hysteresis over a broad range of scan speeds to the ETM and its contact properties. We have thereby revealed improved charge extraction implied by transient photoluminescence studies, faster and less pronounced hysteretic processes as well as better performances for devices with fullerene compared to metal oxide electron contacts. However, only double-layer ETM structures lead to negligible photocurrent hysteresis and highest device efficiencies. A champion stabilized PCE of 18.0 % was achieved by the combination of TiO$_2$ and PCBM as electron contact. Current-voltage measurements indicate strongly reduced recombination losses for the TiO$_2$/PCBM contact design and we suppose multiple originating effects: (I) reduction of shunt paths through the fullerene to the ITO layer, (II) improved hole blocking by the additional wide band-gap metal oxide and (III) decreased charge transport losses due to an energetically more favorable contact, with the latter two being supported by photoelectron spectroscopy measurements. The demonstrated improvements are independent of

the contact polarity or the architecture, meaning that bilayer or even multi-layer selective contacts could be a general design guideline for perovskite solar cells.

Experimental

Deposition of the electron transport materials

The fullerene derivatives $PC_{60}BM$ (99.5 %, Solenne BV) and $IC_{60}MA$ (>99 %, Lumtec) were spin coated in N_2-atmosphere from 10 mg/ml solutions in anhydrous chlorobenzene at 2000 rpm for 30 s. The samples were subsequently annealed at 100 °C for 10 min. Alternatively, 35 nm of C_{60} were thermally evaporated at a base pressure of 10^{-6} mbar and a crucible temperature of 385 °C which resulted in a rate of 0.2 Å/s. No further post-treatment was conducted after C_{60} evaporation.

A dispersion of TiO_2 nanoparticles and titanium diisopropoxide bis(acetylacetonate) (TiAcAc, 75 wt. % in isopropanol, Sigma-Aldrich) in anhydrous ethanol (Sigma-Aldrich) was prepared following a reported synthesis procedure.[23] In brief, 0.25 ml of anhydrous $TiCl_4$ (99.9 %, Sigma-Aldrich) were added dropwise while stirring to 1 ml of anhydrous ethanol and 5 ml of anhydrous benzyl alcohol (99.8 %, Sigma-Aldrich). The solution was kept stirring at 80 °C for 9 h, afterwards cooled down to room temperature and mixed in a 1:9 volume ratio with diethyl ether to precipitate the TiO_2 nanoparticles. After centrifuging of each 10 ml of this mixture at 6000 rpm for 5 min, the precipitate was washed with acetone and redispersed in 20 ml of anhydrous ethanol. Finally, 5 µl TiAcAc were added per 20 ml of the dispersion.

To deposit TiO_2 as an electron selective contact, the above described dispersion was spin coated two times on top of a sample at 1000 rpm for 40 s in ambient air. After a thermal annealing at 150 °C for 30 min, the complete procedure was repeated to double the final film thickness.

To deposit SnO_2 as an electron selective material, samples were spin coated in ambient air with 4 mg $SnCl_2 \cdot 2H_2O$ (>99.995 %, Sigma-Aldrich) in 1 ml of anhydrous ethanol (Sigma-Aldrich) at 2000 rpm for 40 s and afterwards annealed at 180 °C for 60 min according to Ke et al.[24]

For devices incorporating the double-layer ETM structured, the respective metal oxide and a PCBM layer were successively deposited as described above for the single-layer electron contacts.

Perovskite Solar Cell Preparation

Regular planar perovskite solar cells were prepared as a layer stack of glass/ITO/ETM/$CH_3NH_3PbI_3$/spiro-OMeTAD/Au. Patterned ITO coated glass substrates (R = 15 Ω/sq., Lumtec) were cleaned sequentially for 15 min with detergent, acetone and isopropanol in ultrasonic bath. Deposition of the electron selective contact is described in the related section above. Further processing was performed in a N_2 filled glovebox.

350 nm thick $CH_3NH_3PbI_3$ layers were prepared according to a marginally modified published method.[38] 1.1 M CH_3NH_3I (MAI, Dyenamo) and 1.1 M PbI_2 (99.99 %, TCI) were first dissolved in a cosolvent of γ-butyrolactone (GBL, ≥99 %, Sigma Aldrich) and dimethyl sulfoxide (DMSO, Sigma-Aldrich) with 7:3 volume ratio and left stirring at 60 °C for 12 h. Glovebox atmosphere temperature was elevated before perovskite deposition to around 28 °C. The precursor solution was then spin coated upon the samples in three consecutive steps at 1000 rpm for 10 s, 2000 rpm for 20 s and 5000 rpm for 10 s with 150 µl of toluene poured during the third spinning stage. A subsequent annealing at 100 °C for 10 min completed the perovskite layer preparation.

Prior to depositing the hole conductor 2,2',7,7'-tetrakis(N,N-di-4-methoxy-phenyl-amino)-9,9'-spirobifluorene (spiro-OMeTAD, Merck), 36.2 mg of spiro-OMeTAD were dissolved in 1 ml of chlorobenzene (CBZ), 8.8 µL of a bis(trifluoromethane) sulfonimide lithium salt (LiTFSI, Lumtec) stock solution (520 mg/ml in acetonitrile), 14.5 µL of a tris(bis(trifluoromethylsulfonyl)imide)) (FK209,

Dyenamo) stock solution (300 mg/ml in acetonitrile) and 14.4 μL of 4-tert-butylpyridine (Sigma-Aldrich). The spiro-OMeTAD solution containing the doping agents was spin coated onto the samples at 1800 rpm for 30 s.

Finally, 80 nm gold was thermally evaporated through shadow masks, defining active areas of 16 mm², at a base pressure of 10^{-6} mbar and a rate of 0.7 Å/s.

Measurements

Current-voltage measurements were conducted in air using a "Steuernagel Lichtechnik" sun simulator, mimicking AM 1.5G spectra and adjusted to 100 mW/cm² by measuring the short circuit current of a calibrated silicon solar cell (Fraunhofer ISE). The silicon reference and the perovskite solar cells were temperature controlled to 25°C during measurement. The active area of 0.16 cm² was defined by the overlap of orthogonal ITO and gold patterns, both 4 mm in width. Perovskite solar cells were scanned with a digital source meter (Keithley Model 2400) in two consecutive sweeps without pre-biasing of the device, first from -0.5 V to 1.3 V and immediately afterwards in reverse from 1.3 V to -0.5 V. The scan rate was varied as discussed between 277 and 2500 mV/s. To avoid underestimations of the active area, J-V measurements were partially performed with 0.10 cm² shadow masks. As a result of the discrepancies in measured J_{SC} values between masked and unmasked devices, an area correction factor was derived which is included for all unmasked J-V scans. Measurements in N_2 atmosphere were performed as before but under the illumination of simulated AM 1.5G solar light from an Oriel class ABB solar simulator system, adjusted with the same silicon reference cell. For MPP tracking measurements, the power output of a device was continuously feedback controlled using a homemade software. Starting at the voltage of the MPP of the reverse scan at 1666 mV/s, steps of +10 mV, 0 mV and -10 mV were added to the actual voltage and the current density of the device was traced at each operating point for 1 s. The bias point with the highest average power output during the last 0.5 s of each scan was then selected as the new MPP for the subsequent iteration.

The ultraviolet photoelectron spectroscopy (UPS) measurements were performed in an UHV system at base pressures of 1×10^{-9} mbar. He-UPS measurements with an excitation energy of 21.2 eV were conducted to determine the ionization potentials. Since He-UPS is very surface sensitive and contaminations such as adsorbates could influence the work function of the samples, we additionally performed measurements with 6.5 eV excitation energy by a Xe-XBO-lamp. The work function was determined by fitting a Boltzmann sigmoid function to the secondary electron cut-off, whereas the ionization potential was identified by extrapolating the guiding line of the Fermi edge. All electron contacts characterized by UPS were prepared as described for the solar cell preparation in a glass/ITO/ETM structure. After deposition, all substrates were exposed to air for few minutes during the transport to the UHV system.

For transient photoluminescence (TRPL) measurements, fully prepared perovskite solar cells were excited in air by a pulsed laser at 405 nm wavelength and 50 nJ/cm² fluence. No external bias was applied during the experiment.

External quantum efficiency (EQE) was measured in nitrogen atmosphere using an Oriel Instrument's QEPVSI-b system with a Xenon arc lamp (Newport 300 W, 66902) chopped at 35.5 Hz and a monochromatic instrument (Newport Cornerstone 260). The illumination beam size on the sample is 2.5 x 2.5 mm² and measurements were performed in a wavelength range from 300 to 850 nm with 10 nm steps, controlled by TracQ™-Basic software. The external quantum efficiency was measured without background illumination or applied bias voltage.

Modulated surface photovoltage (SPV) measurements were carried out in air with a fixed capacitor arrangement. The samples were illuminated through a quartz cylinder partially covered with SnO_2:F as a reference electrode while an about 10-30 µm thick mica sheet was used as a dielectric spacer to the perovskite surface. The respective perovskite sample was connected via the ITO front electrode. A halogen lamp was chopped at a frequency of 8 Hz and monochromated by a quartz prism to provide spectral measurements in an energy range from 1.4 1.8 eV. A double phase lock in amplifier (EG & G, 7260 DSP) was used to record the modulated signals as an in-phase and a phase shifted by 90° signal. The tail state energies E_T were obtained by fitting the in-phase SPV signals at the leading edge below the band gap energy with an exponential expression reported elsewhere.[43]

Scanning electron micrograph (SEM) pictures were recorded with a Hitachi S-4100 at 5kV acceleration voltage and 30k or 50k magnification for top view or cross section images respectively. Top view images were processed with "GNU Image Manipulation Program" software to optimize edge detection and grain size determination via the software "Gwyddion".

References

1. National Renewable Energy Laboratory. Efficiency Chart. (2016). at <http://www.nrel.gov/ncpv/images/efficiency_chart.jpg>

2. ISE Fraunhofer. Photovoltaics Report 2016. (2016). at <http://www.ise.fraunhofer.de/en/downloads-englisch/pdf-files-englisch/photovoltaics-report-slides.pdf>

3. Leijtens, T. *et al.* Stability of Metal Halide Perovskite Solar Cells. *Adv. Energy Mater.* **5,** 1500963 (2015).

4. Saliba, M. *et al.* Incorporation of rubidium cations into perovskite solar cells improves photovoltaic performance. *Science (80-.).* **354,** 206–209 (2016).

5. Bella, F. *et al.* Improving efficiency and stability of perovskite solar cells with photocurable fluoropolymers. *Science (80-.).* **354,** 203–206 (2016).

6. Wang, Q., Dong, Q., Li, T., Gruverman, A. & Huang, J. Thin Insulating Tunneling Contacts for Efficient and Water-Resistant Perovskite Solar Cells. *Adv. Mater.* **28,** 6734–6739 (2016).

7. IMEC. IMEC News - Stacked Perovskite/CIGS Solar Module Achieves Unprecedented Efficiency at 17.8 Percent. at <http://www2.imec.be/be_en/press/imec-news/perovskite-eng.html>

8. Oxford Photovoltaics. Oxford PV acquires thin-film development line for perovskite scale-up. (2016). at <http://www.oxfordpv.com/News/20161114-Oxford-PV-acquires-thin-film-development-line-for-perovskite-scale-up>

9. Heo, J. H. *et al.* Highly efficient low temperature solution processable planar type CH3NH3PbI3 perovskite flexible solar cells. *J. Mater. Chem. A* **4,** 1572–1578 (2016).

10. Li, Y. *et al.* High-efficiency robust perovskite solar cells on ultrathin flexible substrates. *Nat.*

Commun. **7,** 10214 (2016).

11.   Albrecht, S. *et al.* Monolithic Perovskite / Silicon-Heterojunction Tandem Solar Cells Processed at Low Temperature. *Energy Environ. Sci.* **9,** 81–88 (2016).

12.   Werner, J. *et al.* Efficient Near-Infrared-Transparent Perovskite Solar Cells Enabling Direct Comparison of 4-Terminal and Monolithic Perovskite/Silicon Tandem Cells. *ACS Energy Lett.* **1,** 474–480 (2016).

13.   Eperon, G. E. *et al.* Perovskite-perovskite tandem photovoltaics with optimized band gaps. *Science (80-.).* **354,** 861–865 (2016).

14.   Meng, L., You, J., Guo, T. F. & Yang, Y. Recent Advances in the Inverted Planar Structure of Perovskite Solar Cells. *Acc. Chem. Res.* **49,** 155–165 (2016).

15.   Heo, J. H., Han, H. J., Kim, D., Ahn, T. K. & Im, S. H. Hysteresis-less inverted CH3NH3PbI3 planar perovskite hybrid solar cells with 18.1% power conversion efficiency. *Energy Environ. Sci.* **8,** 1602–1608 (2015).

16.   Zhou, Y., Game, O. S., Pang, S. & Padture, N. P. Microstructures of Organometal Trihalide Perovskites for Solar Cells: Their Evolution from Solutions and Characterization. *J. Phys. Chem. Lett.* **6,** 4827–4839 (2015).

17.   Kim, H.-S. *et al.* Control of I – V Hysteresis in CH 3 NH 3 PbI 3 Perovskite Solar Cell. *J. Phys. Chem. Lett.* **6,** 4633–4639 (2015).

18.   Zhou, H. *et al.* Interface engineering of highly efficient perovskite solar cells. *Science (80-.).* **345,** 542–546 (2014).

19.   Hu, Q. *et al.* Engineering of Electron-Selective Contact for Perovskite Solar Cells with Efficiency Exceeding 15%. *ACS Nano* **8,** 10161–10167 (2014).

20.   Huang, C. *et al.* Efficient Planar Perovskite Solar Cells with Reduced Hysteresis and Enhanced Open Circuit Voltage by Using PW 12 –TiO 2 as Electron Transport Layer. *ACS Appl. Mater. Interfaces* **8,** 8520–8526 (2016).

21.   Wang, H.-H. *et al.* Improving the TiO 2 electron transport layer in perovskite solar cells using acetylacetonate-based additives. *J. Mater. Chem. A* **2,** 6310 (2015).

22.   Anaraki, E. H. *et al.* Highly efficient and stable planar perovskite solar cells by solution-processed tin oxide. *Energy Environ. Sci.* **9,** 3128–3134 (2016).

23.   Wojciechowski, K., Saliba, M., Leijtens, T., Abate, A. & Snaith, H. J. Sub-150 °C processed meso-superstructured perovskite solar cells with enhanced efficiency. *Energy Environ. Sci.* **7,** 1142–1147 (2014).

24.   Ke, W. *et al.* Low-Temperature solution-processed tin oxide as an alternative electron transporting layer for efficient perovskite solar cells. *J. Am. Chem. Soc.* **137,** 6730–6733 (2015).

25.   Wojciechowski, K. *et al.* Heterojunction Modification for Highly Efficient Organic–Inorganic Perovskite Solar Cells. *ACS Nano* **8,** 12701–12709 (2014).

26.   Abrusci, A. *et al.* High-performance perovskite-polymer hybrid solar cells via electronic coupling with fullerene monolayers. *Nano Lett.* **13,** 3124–3128 (2013).

27.   Tao, C. *et al.* 17.6% stabilized efficiency in low-temperature processed planar perovskite solar cells. *Energy Environ. Sci.* **8,** 2365–2370 (2015).

28.   Xu, J. *et al.* Perovskite-fullerene hybrid materials suppress hysteresis in planar diodes. *Nat.*

Commun. **6,** 7081 (2015).

29. van Reenen, S., Kemerink, M. & Snaith, H. J. Modeling Anomalous Hysteresis in Perovskite Solar Cells. *J. Phys. Chem. Lett.* **6,** 3808–3814 (2015).

30. Albrecht, S. *et al.* On the Efficiency of Charge Transfer State Splitting in Polymer:Fullerene Solar Cells. *Adv. Mater.* **26,** 2533–2539 (2014).

31. He, Y., Chen, H. Y., Hou, J. & Li, Y. Indene - C60 bisadduct: A new acceptor for high-performance polymer solar cells. *J. Am. Chem. Soc.* **132,** 1377–1382 (2010).

32. Ahn, N., Kang, S. M., Lee, J., Choi, M. & Park, N.-G. Thermodynamic regulation of CH 3 NH 3 PbI 3 crystal growth and its effect on photovoltaic performance of perovskite solar cells. *J. Mater. Chem. A* **3,** 19901–19906 (2015).

33. Correa Baena, J. P. *et al.* Highly efficient planar perovskite solar cells through band alignment engineering. *Energy Environ. Sci.* **8,** 2928–2934 (2015).

34. Ishiyama, N., Kubo, M., Kaji, T. & Hiramoto, M. Doping-based control of the energetic structure of photovoltaic co-deposited films. *Appl. Phys. Lett.* **99,** 1–5 (2011).

35. Nakanishi, R., Nogimura, A., Eguchi, R. & Kanai, K. Electronic structure of fullerene derivatives in organic photovoltaics. *Org. Electron.* **15,** 2912–2921 (2014).

36. Ogomi, Y. *et al.* CH3NH3SnxPb(1–x)I3 Perovskite Solar Cells Covering up to 1060 nm. *J. Phys. Chem. Lett.* **5,** 1004–1011 (2014).

37. Bi, C. *et al.* Non-wetting surface-driven high-aspect-ratio crystalline grain growth for efficient hybrid perovskite solar cells. *Nat. Commun.* **6,** 7747 (2015).

38. Jeon, N. J. *et al.* Solvent engineering for high-performance inorganic-organic hybrid perovskite solar cells. *Nat. Mater.* **13,** 897–903 (2014).

39. Wolansky, G. & Marmur, A. Apparent contact angles on rough surfaces: The Wenzel equation revisited. *Colloids Surfaces A Physicochem. Eng. Asp.* **156,** 381–388 (1999).

40. Salim, T. *et al.* Perovskite-based solar cells: impact of morphology and device architecture on device performance. *J. Mater. Chem. A* **3,** 8943–8969 (2015).

41. Momblona, C. *et al.* Efficient vacuum deposited p-i-n and n-i-p perovskite solar cells employing doped charge transport layers. *Energy Environ. Sci.* **9,** 3456–3463 (2016).

42. Minemawari, H. *et al.* Inkjet printing of single-crystal films. *Nature* **475,** 364–367 (2011).

43. Macor, L. *et al.* Photoinduced charge separation in donor–acceptor spiro compounds at metal and metal oxide surfaces: application in dye-sensitized solar cell. *RSC Adv.* **2,** 4869 (2012).

44. Brenner, T. M., Egger, D. A., Kronik, L., Hodes, G. & Cahen, D. Hybrid organic—inorganic perovskites: low-cost semiconductors with intriguing charge-transport properties. *Nat. Rev. Mater.* **1,** 15007 (2016).

45. Owino Juma, A. *et al.* Role of chlorine in In2S3 for band alignment at nanoporous-TiO2/In2S3 interfaces. *J. Appl. Phys.* **114,** 2–7 (2013).

46. Yin, W.-J., Yang, J.-H., Kang, J., Yan, Y. & Wei, S.-H. Halide perovskite materials for solar cells: a theoretical review. *J. Mater. Chem. A* **3,** 8926–8942 (2015).

47. Shao, Y., Yuan, Y. & Huang, J. Correlation of energy disorder and open-circuit voltage in hybrid perovskite solar cells. *Nat. Energy* **1,** 15001 (2016).

48. Min, J. *et al.* Interface Engineering of Perovskite Hybrid Solar Cells with Solution-Processed

Perylene–Diimide Heterojunctions toward High Performance. *Chem. Mater.* **27,** 227–234 (2015).

49. Jacobsson, T. J. *et al.* Unreacted PbI 2 as a Double-Edged Sword for Enhancing the Performance of Perovskite Solar Cells. *J. Am. Chem. Soc.* **138,** 10331–10343 (2016).

50. Unger, E. L. *et al.* Hysteresis and transient behavior in current–voltage measurements of hybrid-perovskite absorber solar cells. *Energy Environ. Sci.* **7,** 3690–3698 (2014).

51. Tress, W. *et al.* Understanding the rate-dependent J–V hysteresis, slow time component, and aging in CH 3 NH 3 PbI 3 perovskite solar cells: the role of a compensated electric field. *Energy Environ. Sci.* **8,** 995–1004 (2015).

52. Chen, B. *et al.* Impact of Capacitive Effect and Ion Migration on the Hysteretic Behavior of Perovskite Solar Cells. *J. Phys. Chem. Lett.* **6,** 4693–4700 (2015).

53. Zarazua, I., Bisquert, J. & Garcia-Belmonte, G. Light-Induced Space-Charge Accumulation Zone as Photovoltaic Mechanism in Perovskite Solar Cells. *J. Phys. Chem. Lett.* **7,** 525–528 (2016).

54. Shao, Y., Xiao, Z., Bi, C., Yuan, Y. & Huang, J. Origin and elimination of photocurrent hysteresis by fullerene passivation in CH3NH3PbI3 planar heterojunction solar cells. *Nat. Commun.* **5,** 5784 (2014).

55. Wu, Y. *et al.* Perovskite solar cells with 18.21% efficiency and area over 1 cm2 fabricated by heterojunction engineering. *Nat. Energy* **1,** 16148 (2016).

56. Zhang, H. *et al.* Dynamic interface charge governing the current–voltage hysteresis in perovskite solar cells. *Phys. Chem. Chem. Phys.* **17,** 9613–9618 (2015).

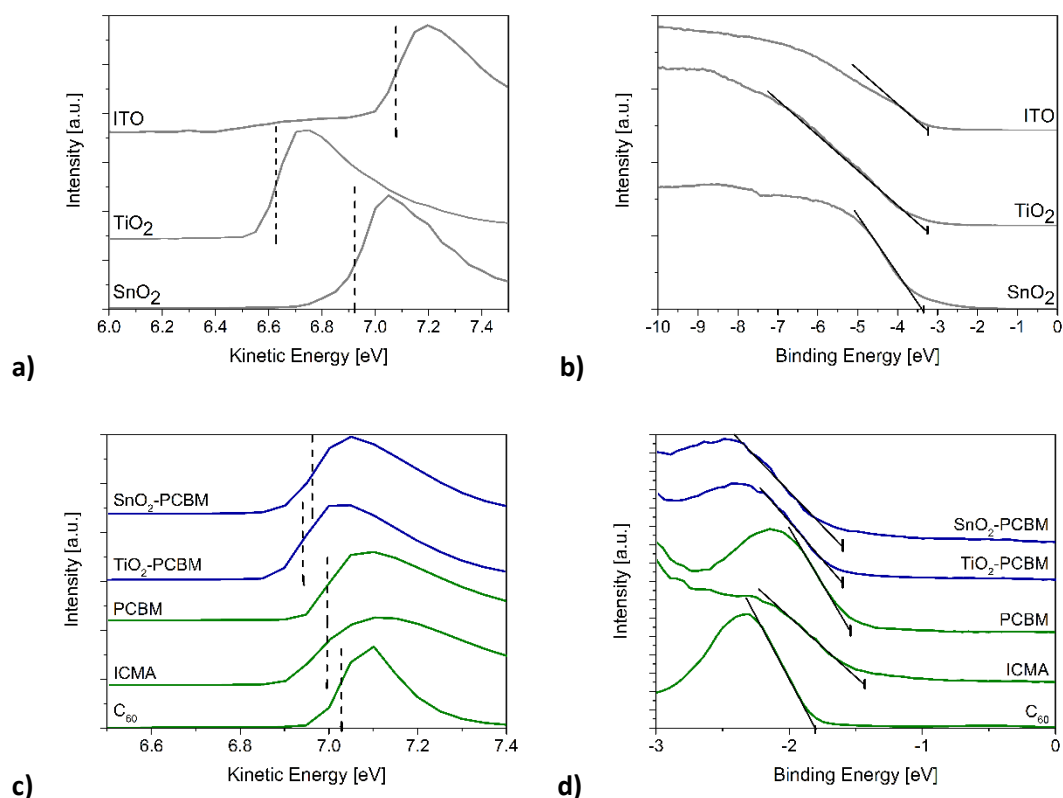# Supplementary Informations

a)

b)

c)

d)

Figure S1. UPS measurements to determine (a) the secondary electron cut-off (SECO) and (b) the Fermi-edge of the metal oxides. (c) and (d) present the respective characteristics for organic single- and double-layer ETMs.

ETM	Work function from SECO	Fermi Edge	Ionization potential
ITO	-4.6 eV	-3.2 eV	-7.8 eV
TiO_2	-4.1 eV	-3.2 eV	-7.3 eV
SnO_2	-4.45 eV	-3.35 eV	-7.8 eV
ICMA	-4.5 eV	-1.45 eV	-5.95 eV
C_{60}	-4.55 eV	-1.8 eV	-6.35 eV
PCBM	-4.5 eV	-1.55 eV	-6.05 eV
SnO_2-PCBM	-4.45 eV	-1.65 eV	-6.1 eV
TiO_2-PCBM	-4.45 eV	-1.65 eV	-6.1 eV

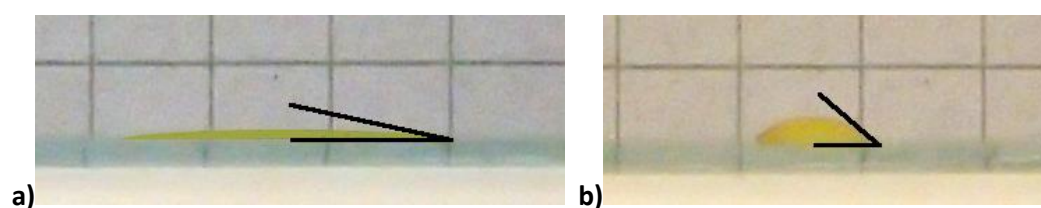**Table S1. Work function and Fermi edge energies corresponding to Figure S1 as well as resulting ionization potentials.**

a)

b)

Figure S2. Droplets of 10 µl of the perovskite precursor solution on (a) glass/ITO/TiO_2 and (b) glass/ITO/PCBM.

Surface Roughness	ITO	TiO₂	SnO₂	C60	PCBM	SnO₂-PCBM	TiO₂-PCBM
RMS [nm]	3	3	3	16	4	2	2

Table S2. Root-mean-square (RMS) values of the surface roughness of different ETMs on ITO determined by atomic force microscopy.
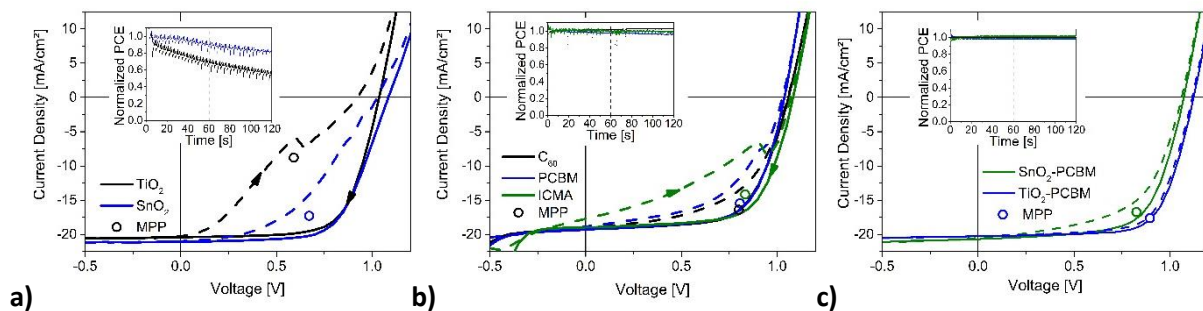

a)   b)   c)

Figure S3. Current density-voltage (J-V) characteristics under illumination and maximum power points (MPP) after 60 s MPP tracking of perovskite solar cells with (a) TiO₂ or SnO₂ and (b) ICMA, C60 or PCBM as single-layer ETM. Corresponding curves for devices with a double-layer ETM structure of SnO₂-PCBM and TiO₂-PCBM are depicted in panel (c). The insets show maximum power point tracking measurements of the solar cells.
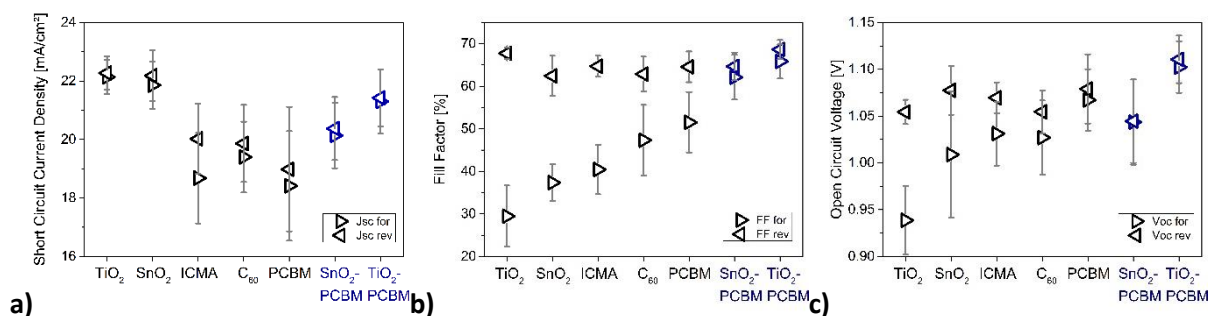

a)   b)   c)

Figure S4. Parameters (a) J_SC, (b) fill factor and (c) V_OC averaged separately for forward and reverse scans at 1666 mV/s sweep rate for perovskite solar cells under illumination with different ETMs averaged over all devices.
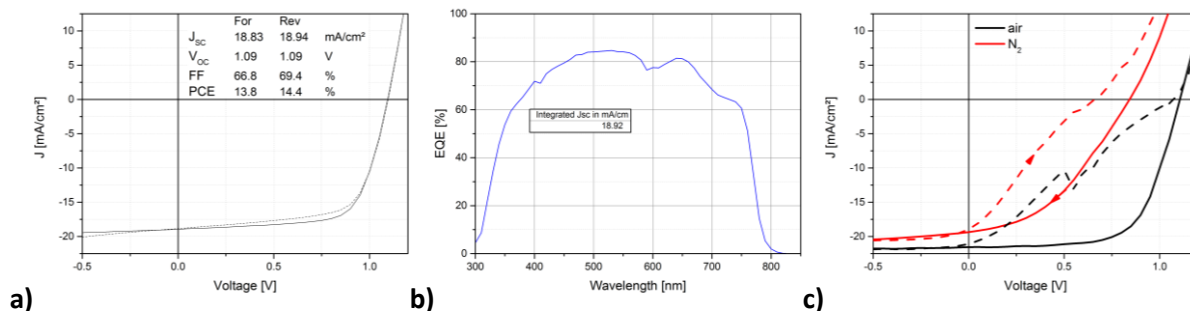

a)   b)   c)

Figure S5. (a) J-V-curve measured in N₂ atmosphere and 1666 mV/s scan speed corresponding to the champion device shown in Figure 4 (b). (b) Respective external quantum efficiency also determined in N₂ atmosphere. (c) J-V-measurements of a TiO₂ single-layer ETM device in air and N₂ atmosphere, both at 1666 mV/s.

The J-V-curves of devices measured in N_2 atmosphere differed strongly from those obtained in air. As an example Figure 4 (b) and Figure S5 (a) show J-V-curves of the same device, measured on the same day but in air and N_2 respectively. As the external quantum efficiency (EQE) measurement was performed in N_2 (Figure S5 (b)), we were able to confirm the J_{SC} value of the corresponding J-V-scan (Figure S5 (a)). As the reduction of J_{SC} in N_2 compared to measurements in air is reversible and was observed more pronounced for devices incorporating metal oxides (Figure S5 (c)), we suggest that oxygen in the environment plays an important role in this device architecture for the Spiro-OMeTAD hole and the metal oxide electron selective layers.